Neurosurgery

2017

Optical-Sectioning Microscopy of Protoporphyrin Ix Fluorescence in Human Gliomas: Standardization and Quantitative Comparison With Histology

Linpeng Wei

Ye Chen

Chengbo Yin

Sabine Borwege

Nader Sanai
Barrow Neurological Institute, nader.sanai@bnaneuro.net

See next page for additional authors

Follow this and additional works at: https://scholar.barrowneuro.org/neurosurgery

Authors
Linpeng Wei, Ye Chen, Chengbo Yin, Sabine Borwege, Nader Sanai, and Jonathan T.C. Liu

Optical-sectioning microscopy of protoporphyrin IX fluorescence in human gliomas: standardization and quantitative comparison with histology

Linpeng Wei
Ye Chen
Chengbo Yin
Sabine Borwege
Nader Sanai
Jonathan T. C. Liu

SPIE.

Optical-sectioning microscopy of protoporphyrin IX fluorescence in human gliomas: standardization and quantitative comparison with histology

Linpeng Wei,[a] Ye Chen,[a] Chengbo Yin,[a] Sabine Borwege,[b] Nader Sanai,[b] and Jonathan T. C. Liu[a,*]
[a]University of Washington, Department of Mechanical Engineering, Seattle, Washington, United States
[b]Barrow Neurological Institute, St. Joseph's Hospital, Phoenix, Arizona, United States

Abstract. Systemic delivery of 5-aminolevulinic acid leads to enhanced fluorescence image contrast in many tumors due to the increased accumulation of protoporphyrin IX (PpIX), a fluorescent porphyrin that is associated with tumor burden and proliferation. The value of PpIX-guided resection of malignant gliomas has been demonstrated in prospective randomized clinical studies in which a twofold greater extent of resection and improved progression-free survival have been observed. In low-grade gliomas and at the diffuse infiltrative margins of all gliomas, PpIX fluorescence is often too weak to be detected with current low-resolution surgical microscopes that are used in operating rooms. However, it has been demonstrated that high-resolution optical-sectioning microscopes are capable of detecting the sparse and punctate accumulations of PpIX that are undetectable via conventional low-power surgical fluorescence microscopes. To standardize the performance of high-resolution optical-sectioning devices for future clinical use, we have developed an imaging phantom and methods to ensure that the imaging of PpIX-expressing brain tissues can be performed reproducibly. *Ex vivo* imaging studies with a dual-axis confocal microscope demonstrate that these methods enable the acquisition of images from unsectioned human brain tissues that quantitatively and consistently correlate with images of histologically processed tissue sections. © *2017 Society of Photo-Optical Instrumentation Engineers (SPIE)* [DOI: 10.1117/1.JBO.22.4.046005]

Keywords: optical-sectioning microscopy; protoporphyrin IX; standardization phantoms.

Paper 160802R received Nov. 29, 2016; accepted for publication Mar. 27, 2017; published online Apr. 13, 2017.

1 Introduction

Gliomas are the most common primary malignant brain tumor in adults and are considered one of the deadliest cancers. Patients with glioblastoma [World Health Organization (WHO) Grade IV glioma] have a median survival of 14 months and a 2-year survival rate of 26%, even when optimal treatment is provided.[1,2] Reducing the tumor burden through surgical resection remains the first step in effective glioma management, where studies have shown that more extensive surgical resection is associated with better prognosis.[2–9] Unfortunately, the gross-total resection (GTR) of gliomas [complete resection as assessed by postoperative magnetic resonance imaging (MRI)] is challenging due to the diffuse distribution of glioma cells in which the tumor margins are indistinguishable from the surrounding normal brain under visual inspection.[10] Furthermore, while a number of modern intraoperative techniques (e.g., intraoperative ultrasonography and MRI) have been developed to guide glioma resections, the reported rates of GTR of gliomas remains low, especially for low-grade gliomas (LGG). A major reason is that for most wide-field imaging techniques, the intensity of each low-resolution pixel represents an average signal from a large number of cells, resulting in a low sensitivity to detecting sparse tumor-cell populations in LGGs, as well as at the diffuse margins of all gliomas. Over and above the goal of achieving GTR (based on MRI), there is a need to visualize and quantify tumor burden beyond the radiographic margins as it is well known that glioma cells infiltrate beyond the regions of MRI contrast-enhancement.[11–14]

In recent years, numerous reports have detailed the benefits of fluorescence image-guided surgery for the resection of high-grade gliomas (HGGs) in patients who have been administered 5-aminolevulinic acid (5-ALA), a prodrug that induces the production of protoporphyrin IX (PpIX) as a fluorescent contrast agent.[15–27] PpIX is an endogenous fluorescent substrate in the heme-synthesis pathway and has been shown to preferentially accumulate in glioma cells due to metabolic dysregulation.[28] PpIX emits red fluorescence ($\lambda_{em} = 600$ to 700 nm) when excited with violet light ($\lambda_{ex} = 400$ to 410 nm).[29,30] In glioma patients, this accumulation of PpIX is amplified by delivering an oral dose of 5-ALA several hours prior to surgery.[16] A landmark randomized phase III clinical trial in Europe showed that PpIX-guided surgeries resulted in more complete tumor resections (GTR of 65% versus 36% for the control group), as well as improved patient outcomes (6-month progression free survival rate of 41% versus 21% for the control group).[17] Currently, 5-ALA is approved for neurosurgical use in Europe, Canada, and Japan, and is being used in a number of clinical studies in the United States under Investigational New Drug-approval by the Food and Drug Administration.

In spite of its success for guiding the resection of HGGs, PpIX-guided surgery remains less effective for LGGs mainly due to the aforementioned limited resolution and sensitivity of current low-resolution surgical imaging systems. However, in a pilot study in 2011, Sanai et al. demonstrated that an intraoperative confocal microscope, with the ability to resolve subcellular features, could visualize the sparse subcellular expression of

PpIX in LGG patients treated with 5-ALA.[10] Based on these promising results, our team is developing a handheld video-rate optical-sectioning microscope that is optimized to visualize and quantify subcellular PpIX expression,[31] the characteristics of which (e.g., intensity, density, etc.) are believed to be associated with tumor burden and proliferative index.[32–34] Ultimately, our objective is to provide an intraoperative imaging device that can provide neurosurgeons with real-time histopathological information and quantitative metrics to optimize the extent of resection for improving patient outcomes.

Our device utilizes a dual-axis confocal (DAC) architecture in which the illumination and collection beam paths are spatially separated (Fig. 1). The advantages of the DAC architecture over conventional single-axis confocal microscopes have been discussed previously.[35–42] Preliminary *ex vivo* studies with a prototype DAC microscope have demonstrated that DAC microscopy provides high-contrast images of subcellular PpIX expression in unsectioned human glioma tissues, with qualitative agreement to fluorescence microscopy of slide-mounted histology sections of the same tissue.[43] We have also developed a line-scanned dual-axis confocal (LS-DAC) microscope system that operates at a higher frame rate (15 to 30 fps) to reduce motion artifacts (blurring) during handheld clinical use.[44–46]

In the study described here, our aim was to further improve the clinical translational potential of LS-DAC microscopy, as well as other optical-sectioning microscopy approaches (e.g., single-axis confocal microscopy,[47–49] nonlinear microscopy,[50] structured-illumination microscopy,[51,52] etc.) for intraoperative guidance of glioma resections based on PpIX fluorescence. In particular, two advances have been made: (1) a fluorescent bead phantom has been developed, along with an imaging protocol, to optimize the alignment and performance of optical-sectioning microscopes. This will ensure the acquisition of quantitatively reproducible images of PpIX-expressing brain tissues with the potential to standardize numerous devices in future multisite clinical studies. (2) Completion of a pilot clinical study (*ex vivo* tissues) to demonstrate that the use of our calibration phantom allows for the acquisition of LS-DAC microscopy data that quantitatively correlate with fluorescence histology data, thus further supporting the potential use of LS-DAC microscopy as a real-time, minimally invasive alternative to conventional gold-standard histopathology.

2 Methods

2.1 Line-Scanned Dual-Axis Confocal Microscope

The microscope system (Fig. 1) used in this study is a modified version of a tabletop LS-DAC microscope system described previously.[44,46] In brief, a single-mode fiber-coupled 405-nm diode laser (OBIS-405, Coherent Inc., Santa Clara, California) is collimated and focused into the sample with unity magnification (numerical aperture, NA ~ 0.12). A planoconvex cylindrical lens ($f = 50$ mm, Optosigma, Santa Ana, California) is inserted in the collimated region of the illumination path to intentionally create a large degree of astigmatism, resulting in a focal line that is 500-μm long and 1.4-μm wide [full width at half maximum (FWHM)]. A one-dimensional galvanometric scanning mirror (6210H, Cambridge Technology, Bedford, Massachusetts) scans the focal line laterally (along the x-axis) to create an image that is parallel to the tissue surface (*en face*). The sample rests on a solid immersion lens (SIL, $n = 1.45$) that is mounted on a linear translation stage. The hemispherical SIL performs index matching of the illumination and collection beams as they obliquely propagate from air into the sample. The SIL also acts as a lens that increases the effective NA of the illumination beam from 0.12 to 0.17 (a factor of n).[35] Fluorescence photons generated at the focal line of the illumination beam are imaged by the collection optics, which are oriented off-axis at a half-crossing angle of 30.0 deg with respect to the illumination axis. The collection path images the focal line onto an sCMOS detector (Hamamatsu ORCA Flash 4.0 v2) with 5$\times$ magnification via a pair of lenses ($f_{L1} = 20$ mm; $f_{L2} = 100$ mm). A 600-nm long-pass fluorescence filter (Semrock BLP01-594R-25) is placed in the beam path to filter out the excitation photons ($\lambda = 405$ nm). Raw images were collected via a camera link frame grabber (Firebird 1xCLD, Active Silicon, United Kingdom) at 1000 raw exposures per second (1 ms per exposure). A custom LabVIEW (National Instruments) program was used to crop out and bin the central three lines of each camera frame (corresponding to the image of the focal line) to create a digital confocal slit (19.5 μm in width, corresponding to $\sim$2.7 μm in tissue). These lines were stitched serially in the x direction (see Fig. 1) into *en face* images in real-time at a two-dimensional (2-D) imaging rate of 2 frames per second (fps). As mentioned previously, the LS-DAC microscope is capable of acquiring images at video rates (15 to 30 fps). However, for the purposes of this study, which aimed

Fig. 1 (a) Schematic of the LS-DAC microscope. A cylindrical lens "C" is inserted in the collimated region of the illumination path to transform a point focus into a line focus. The focal line is scanned by the scan mirror in the x direction to create a 2-D *en face* image of the sample (in the x-y plane). The hemispherical SIL acts as a sample holder that is translated along the axial (z) direction by a motorized stage (not shown) to enable volumetric imaging. (b) Zoomed-in view of the LS-DAC microscope near the sample.

to develop a standardizable phantom and quantitative imaging methods, a lower frame rate was utilized to maximize signal-to-noise ratios (SNR) and to demonstrate the feasibility of our methods. Volumetric data were collected by translating the sample holder along the z axis with a motorized linear actuator (TRA12CC, Newport Corperation, Irvine, California).

2.2 System Standardization with an Agarose-Based Fluorescent Bead Phantom

2.2.1 Phantom preparation

Our standardization phantom consists of fluorescent microspheres in an agarose gel. The fluorescence microspheres (19111-2, Fluoresbrite polychromatic red microspheres) used for this phantom are commercially available through Polysciences Inc. (Warrington, Pennsylvania). These polystyrene-based microspheres are National Institute of Standards and Technology (NIST)-traceable size standards and are designed to be optimally excited at a wavelength of near 525 nm, with an emission peak at 565 nm. In this study, the particles are excited with low efficiency at 405 nm, and only the tail of the fluorescence spectrum is collected with a 600-nm long-pass filter. While this causes the detected fluorescence signal to be relatively weak (compared with the fluorescence signal from the beads at their optimal excitation/emission wavelengths), this weaker signal approximates the strength of the PpIX fluorescence seen in glioma tissues from patients who have been administered 5-ALA and allows the alignment and performance of the microscope to be assessed under realistic conditions (*in situ* fluorescence signal levels).

The stock concentration of microspheres (2.5% aqueous suspension) was diluted 40 times in a 0.8% agarose solution (Sigma Aldrich A9539) at 70°C, and the mixture was allowed to solidify while cooling to room temperature.

2.2.2 Phantom-assisted alignment

Because PpIX has an unusually large Stoke's shift ($\lambda_{ex} =$ 405 nm; $\lambda_{em} =$ 625 nm), the proper alignment of the illumination and collection beam paths of the DAC microscope (or any alternative microscope technology) must account for the chromatic differences between these disparate wavelengths. The fluorescent bead phantom developed in this study is used to provide a high-resolution target (the beads are 6 μm in diameter) that may be used to optimize the alignment of the microscope at an illumination and collection wavelength of 405 and >600 nm, respectively. Volumetric imaging data of the phantom are collected to verify that both the sensitivity (SNR) and the three-dimensional spatial resolution (FWHM dimensions of the beads) are uniform across the field of view (FOV), confirming satisfactory alignment of the dual-axis beams with respect to each other (for high resolution) and with respect to the hemispherical SIL (for uniform resolution across the FOV). For clinical use, a method to verify that the performance of an optical-sectioning microscope is reproducible is to measure the SNR and spatial resolution of the microscope in a volumetric phantom. Here, the SNR is calculated as

$$ \text{SNR} = \frac{S - B}{\sigma_B}, \tag{1} $$

where S is the mean of the peak pixel intensity of all beads in an image, B is the mean pixel intensity of the background, and σ_B is the standard deviation of the background signal. Note that the standard deviation of the peak signal from each bead cannot be reliably measured due to the small size of the beads and their spherical geometry, with only a single pixel corresponding to the peak of each bead.

2.3 Ex Vivo Imaging of PpIX-Expressing Human Brain Tissues

2.3.1 Tissue preparation

Glioma tissue samples ($n = 14$) were collected from consenting patients at the Barrow Neurological Institute (Phoenix, Arizona) in accordance with an approved protocol (IRB #10BN159). Patients were orally administered 5-ALA at a concentration of 20 mg/kg 3 h prior to surgery, and brain biopsies obtained during surgery were fixed in 3% paraformaldehyde for 24 h and then stored in 1× phosphate-buffered saline at 4°C before being imaged with a custom LS-DAC microscope. All tissue specimens were obtained from MRI-enhancing regions corresponding to the bulk tumor. After the LS-DAC images were taken, the imaged tissue surfaces were physically sectioned (10 μm in thickness) in the *en face* direction (as close and parallel to the tissue surface as possible) and mounted on standard microscope slides. Histology slides were imaged with a conventional epifluorescence microscope (DMIRB inverted, Leica Inc., Wetzlar, Germany) to visualize intracellular PpIX expression (625-nm emission). In addition, adjacent sections were stained with hematoxylin and eosin (H&E) and imaged with a standard bright-field pathology microscope (Fig. 2).

### 2.3.2 Image acquisition and quantification

For LS-DAC microscopy, volumetric imaging data were collected at three random tissue locations from each tissue specimen. The FOV of the microscopy datasets was 350 μm (x) by 520 μm (y) by 150 μm (z, depth), and the sampling pitch in these three dimensions was 0.79, 0.88, and 0.69 μm, respectively. From each volumetric dataset, 10-μm-thick average-intensity projections (i.e., optical sections) were visualized to simulate images of 10-μm-thick slide-mounted histology sections. For the quantitative comparison study of LS-DAC microscopy versus fluorescence histology, three regions of interest (350 μm by 520 μm) were randomly selected for correlative analysis. Identical microscope settings were used for the imaging of all histology slides.

In this study, we attempted to quantify the density of the expression of punctate and localized spots of PpIX that appear in glioma tissues.[32,53] The density of PpIX expression was quantified using an identical algorithm for both the LS-DAC microscopy and fluorescence histology images. In brief, the algorithm identifies and quantifies the density of localized spots of PpIX that are brighter than the tissue background (mostly autofluorescence) in which the background is assumed (and observed) to be relatively uniform. The quantification algorithm was implemented via a custom MATLAB® script.

1. Based on the intensity histogram of each image, an exponential curve fit was performed on the low-intensity background distribution, and a threshold was defined that corresponded to the 99.5th percentile of the background distribution (area under the curve).
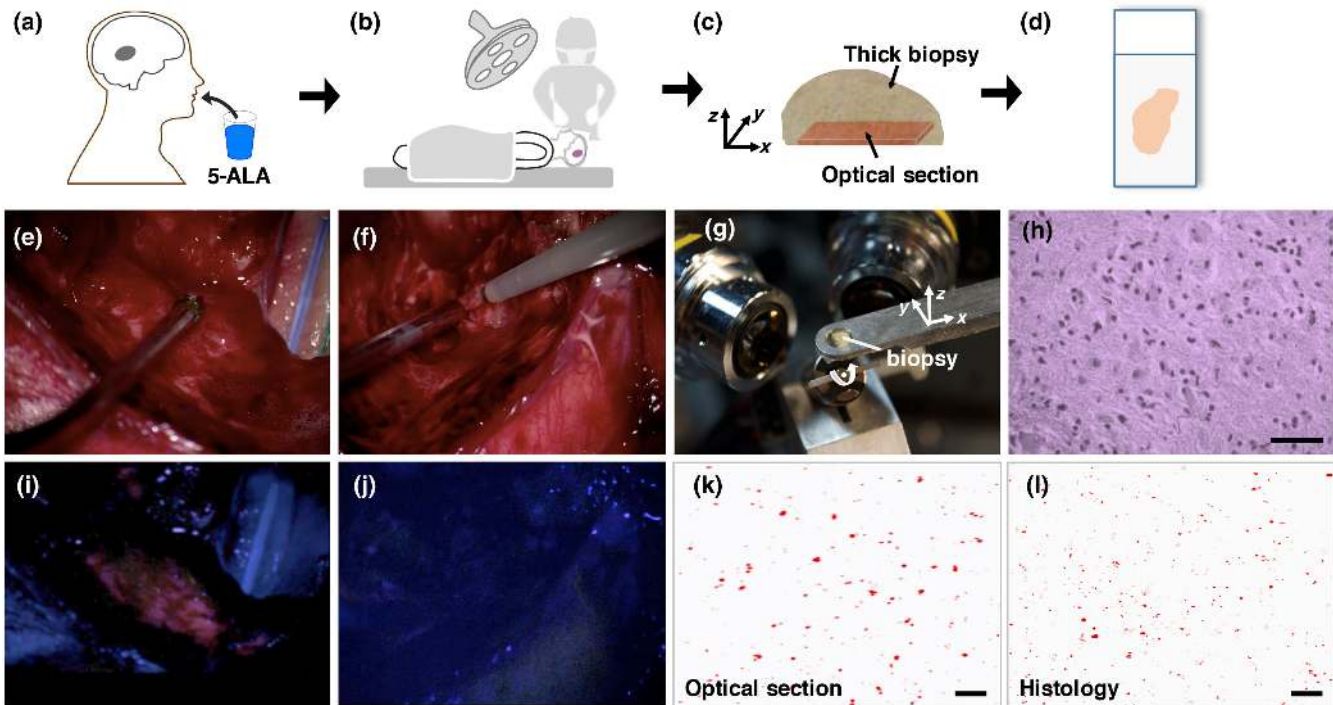
Fig. 2 Workflow of the study with example images. (a, b) Glioma patients were orally administered 5-ALA prior to PpIX-fluorescence-guided surgery. (c) A brain biopsy (grade-III glioma) obtained during the surgical procedure was then imaged with optical-sectioning fluorescence microscopy to obtain images of PpIX expression with subcellular resolution. (d) Corresponding images from histology slides (both H&E staining and PpIX fluorescence) were obtained to validate the optical-sectioning results. (e, f) Example of wide-field intraoperative images from a high-grade glioma (HGG) and a low-grade glioma (LGG) case, respectively, showing that the tumor resembles the surrounding normal tissues under white light imaging in both cases. (g) Photograph of a biopsy specimen placed on the sample holder of a tabletop LS-DAC microscope. (h) Image of an H&E-stained histology section at 40× as a confirmation of the presence of glioma cells in the biopsy specimen. (i, j) Intraoperative wide-field images of PpIX fluorescence (pink color) from the regions shown in (e) and (f), showing that wide-field surgical fluorescence microscopy was capable of detecting PpIX fluorescence from the HGG but not from the LGG. (k) Optical-sectioning microscopy image of the biopsy, showing subcellular PpIX expression. (l) PpIX fluorescence histology image of the same biopsy imaged in (k), showing a similar pattern of PpIX expression. All scale bars represent 50 μm.
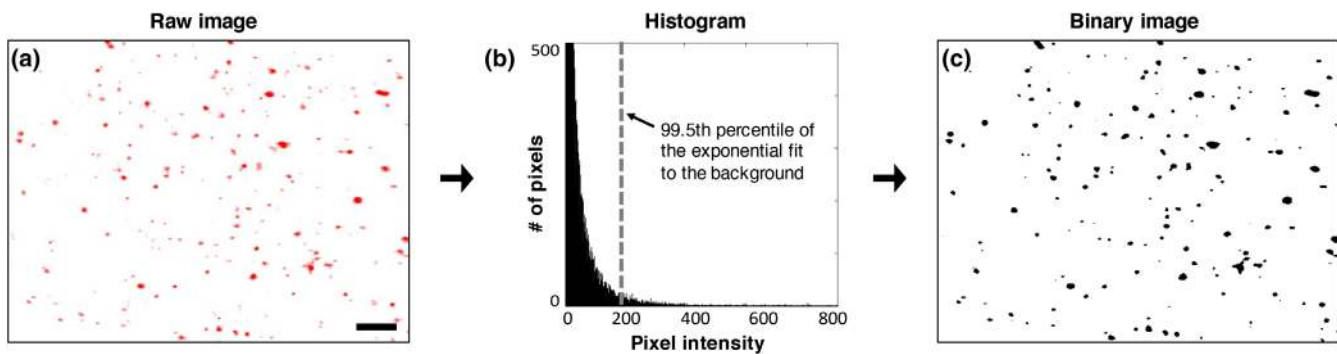
Fig. 3 The same quantification algorithm was used for both LS-DAC images and histology images. (a) Example image of PpIX-expressing glioma tissue obtained with the LS-DAC microscope, the performance of which is standardized with the method detailed in Sec. 2.2. The scale bar represents 50 μm. (b) Histogram of the raw image in which the intensity distribution of the background is approximated as an exponential decay. The dotted line denotes the threshold for segmentation in which pixels with intensities above this threshold are considered "positive" for PpIX expression. (c) A binary image of (a) obtained after segmentation, utilizing a 99.5th percentile threshold to the exponential fit.

2. Once the threshold was identified, a binary image was created by setting all pixels above the threshold as positive [black in Fig. 3(c)] and everything else as negative [white in Fig. 3(c)].

3. A "PpIX-positive spot" was defined as a group of adjacent positive pixels that exhibit an "8-connected" pattern according to a widely used connected-component labeling algorithm[54] (i.e., any two positive pixels that
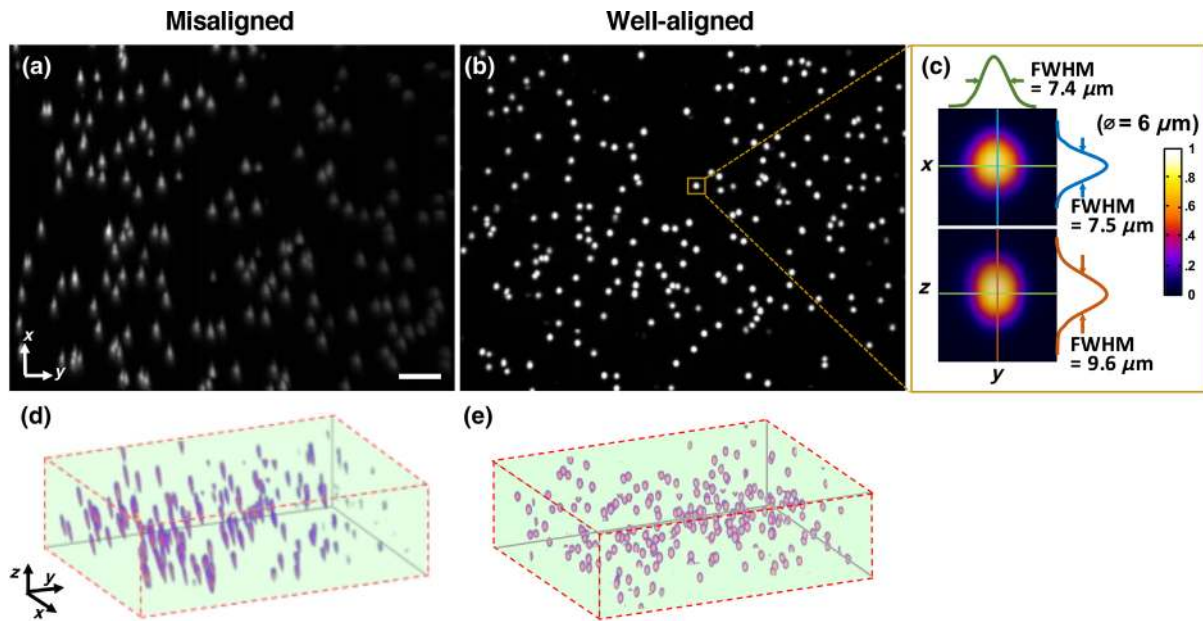
Fig. 4 (a) A maximum-intensity depth projection (along the *z* axis) of a volumetric image of the alignment phantom is shown for a misaligned LS-DAC microscope. (b) A maximum intensity projection of a volumetric image of the phantom (Video 1) is shown from a well-aligned system in which the intensity of the fluorescent beads is uniform across the FOV with <15% deviation (center to edge) and all beads are well-resolved across the entire FOV of 350 μm (*x*) by 520 μm (*y*) by 150 μm (*z*) (Video 1, MPEG, 2.6 MB [URL: http://dx.doi.org/10.1117/1.JBO.22.4.046005.1]). (c) Example cross-sectional views of one bead. The FWHM dimensions of the microsphere allow for the assessment of the spatial resolution of the system. (d, e) Alpha-blending volume renderings of (a and b), respectively, illustrate the uniformity of the detected fluorescence signal from the beads as well as the uniformity of the spatial resolution across the entire FOV. The scale bar represents 50 μm.

share an edge or a vertex will be classified into the same "PpIX-positive" feature). The PpIX density is then defined as the total number of "PpIX-positive spots" per mm^2 (note that each image has an FOV of 350 μm × 520 μm).

3 Results

A total of 14 high- and low-grade glioma samples were imaged during a 15-month period. To ensure the identical performance of the imaging system on different days, the SNR of detection (see Sec. 2.2) was quantified from images of the fluorescent phantom. In addition, the spatial resolution of the system (in all three dimensions) and the uniformity of performance across the FOV were also assessed to confirm the proper alignment of the LS-DAC system (Fig. 4). With the system settings fixed (see Sec. 2.1), the following parameters could be attained in multiple experiments over the entire course of the study (15 months): the SNR of detection was 30.05 dB $\pm$ 3%; the average measured dimensions (FWHM) of the fluorescent beads ($\varnothing = 6$ μm) were 7.5 ± 0.2 μm in the lateral directions and 9.6 ± 0.5 μm in the axial direction (enlarged due to diffraction and minor aberrations). No noticeable fluorescence degradation was observed in the microspheres within a shelf life of 12 months.

For each of the 14 samples, a 10-μm optical section was obtained at three random tissue locations (see Sec. 2.3.2) with the LS-DAC microscope, and the average PpIX density (defined in Sec. 2.2.2) at these three locations was quantified. The same metric (PpIX density) was calculated from the corresponding histology images, and a positive linear relationship

was observed between LS-DAC microscopy versus histology (Fig. 5).

4 Discussion and Conclusion

This study developed a set of tools to enhance the clinical translation of optical-sectioning microscopes for real-time pathology and quantitative surgical guidance of glioma resections. First, a standardization method based on a fluorescent bead phantom was developed. This custom phantom is highly reproducible, stable, and simple to prepare and provides uniform microscopic structures that mimic the sparse and weak fluorescence from 5-ALA-induced PpIX generated by subcellular organelles within glioma tissues. As shown in Fig. 4, this phantom is a valuable tool for ensuring the proper alignment of an optical-sectioning microscope, enabling quantitative characterization of the sensitivity, resolution, and uniformity of the imaging system. As a result, it is possible to obtain reproducible quantitative images of PpIX-expressing brain tissues, which will be necessary to standardize the performance of clinical devices in single-site clinical studies over time and/or in multisite clinical studies. This standardization method is applicable to a variety of optical-sectioning microscopy technologies for intraoperative guidance of glioma resections based on PpIX fluorescence. Second, we showed that quantitative PpIX images obtained with LS-DAC microscopy correlate positively with fluorescence histology, suggesting that LS-DAC microscopy can potentially serve as a minimally invasive and real-time alternative to conventional biopsy and histopathology.

In this study, the density of localized spots of subcellular PpIX expression was chosen as a quantitative metric of interest because it is a potential surrogate measure of tumor burden.
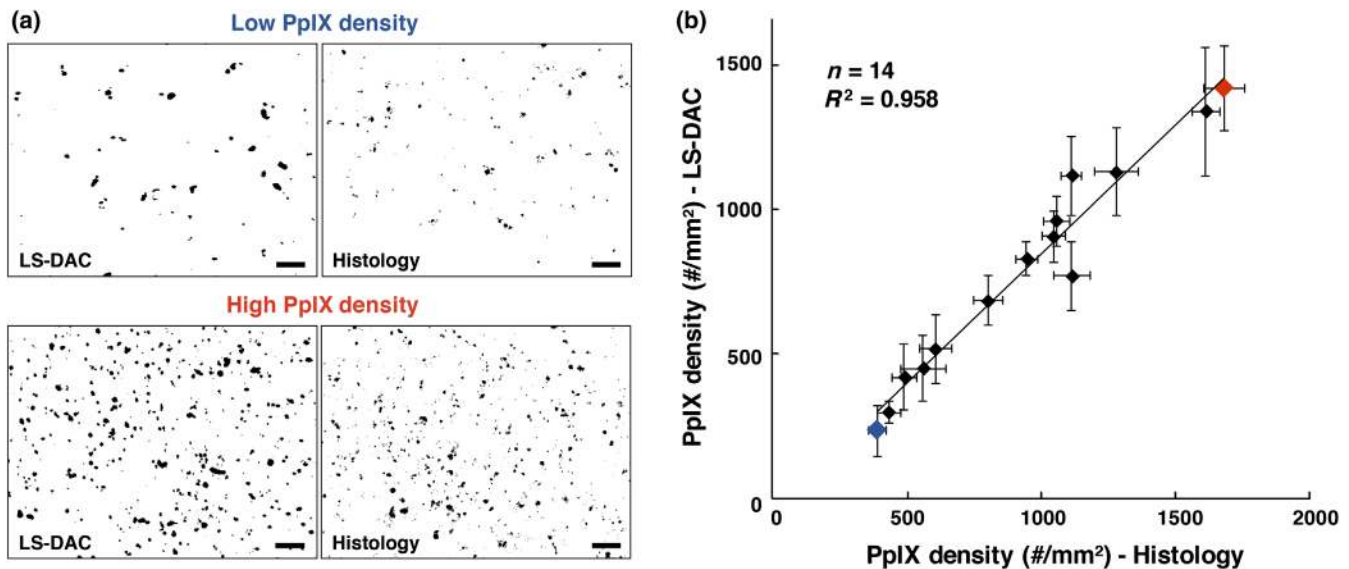
Fig. 5 Quantitative comparison of LS-DAC microscopy images versus corresponding fluorescence histology images in terms of PpIX density. (a) Representative binary images of two of the biopsy samples, one with low PpIX density (blue) and the other with high PpIX density (red). (b) Scatter plot of all 14 glioma specimens obtained over 15 months. Each point on the scatter plot represents the average PpIX density at three randomly chosen locations within each biopsy sample, with the error bars indicating the standard deviation from the measurements. Note that a volumetric dataset (Video 2) was collected at each tissue location, but only a 10-μm optical section at the surface was quantified to simulate a 10-μm slide-mounted histology section. The scale bars represent 50 μm. (Video 2, MPEG, 1.4 MB [URL: http://dx.doi.org/10.1117/1.JBO.22.4.046005.2]).

We show that PpIX density is an objective quantity that can be extracted from both DAC microscopy and histology images, with excellent correlation between these two techniques. Importantly, we note that PpIX density alone may not be an accurate indicator of tumor burden. For example, in some cases, although PpIX density is high, the intensity of the PpIX fluorescence may be low, and/or the size of the PpIX-expressing spots may be smaller than in other specimens. This observation suggests that the intensity and sizes of the signal should also be taken into account when developing a surrogate measure of tumor burden or proliferative index. The observations are consistent with our biological understanding of PpIX generation as the volumetric production of PpIX granular inclusion bodies in brain tumor cells can vary from cell to cell. Ultimately, the clinical significance of these different metrics, for the purposes of optimizing the extent of resection for glioma patients, must be validated through outcome-based clinical studies. Toward this aim, a miniature version of the LS-DAC microscope utilized in this study is currently being assembled and characterized[45] in preparation for future clinical use. In summary, the developments in this study are of value for the clinical translation of handheld intraoperative fluorescence microscopes to guide the resection of gliomas and to improve outcomes for glioma patients.

Disclosures

No conflicts of interest, financial or otherwise, are declared by the authors.

Acknowledgments

References

1. A. Sottoriva et al., "Intratumor heterogeneity in human glioblastoma reflects cancer evolutionary dynamics," *Proc. Natl. Acad. Sci. U. S. A.* **110**(10), 4009–4014 (2013).
2. D. A. Hardesty and N. Sanai, "The value of glioma extent of resection in the modern neurosurgical era," *Front. Neurol.* **3**, 140 (2012).
3. R. Ahmadi et al., "Long-term outcome and survival of surgically treated supratentorial low-grade glioma in adult patients," *Acta Neurochir.* **151**(11), 1359 (2009).
4. J. S. Smith et al., "Role of extent of resection in the long-term outcome of low-grade hemispheric gliomas," *J. Clin. Oncol.* **26**(8), 1338–1345 (2008).
5. E. B. Claus et al., "Survival rates in patients with low-grade glioma after intraoperative magnetic resonance image guidance," *Cancer* **103**(6), 1227–1233 (2005).
6. S. L. Hervey-Jumper and M. S. Berger, "Role of surgical resection in low- and high-grade gliomas," *Curr. Treat. Options Neurol.* **16**(4), 284 (2014).
7. N. Sanai et al., "An extent of resection threshold for newly diagnosed glioblastomas," *J. Neurosurg.* **115**(1), 3–8 (2011).
8. G. E. Keles, K. R. Lamborn, and M. S. Berger, "Low-grade hemispheric gliomas in adults: a critical review of extent of resection as a factor influencing outcome," *J. Neurosurg.* **95**(5), 735–745 (2001).
9. N. Sanai, M. Y. Polley, and M. S. Berger, "Insular glioma resection: assessment of patient morbidity, survival, and tumor progression," *J. Neurosurg.* **112**(1), 1–9 (2010).
10. N. Sanai et al., "Intraoperative confocal microscopy in the visualization of 5-aminolevulinic acid fluorescence in low-grade gliomas," *J. Neurosurg.* **115**(4), 740–748 (2011).
11. N. Galldiks et al., "Volumetry of [(11)C]-methionine PET uptake and MRI contrast enhancement in patients with recurrent glioblastoma multiforme," *Eur. J. Nucl. Med. Mol. Imaging* **37**(1), 84–92 (2010).
12. L. D. Lunsford, A. J. Martinez, and R. E. Latchaw, "Magnetic resonance imaging does not define tumor boundaries," *Acta Radiol. Suppl.* **369**, 154–156 (1986).
13. J. Pallud et al., "Diffuse low-grade oligodendrogliomas extend beyond MRI-defined abnormalities," *Neurology* **74**(21), 1724–1731 (2010).

14. D. O. Kamson et al., "Tryptophan PET in pretreatment delineation of newly-diagnosed gliomas: MRI and histopathologic correlates," *J. Neurooncol.* **112**(1), 121–132 (2013).

15. W. Stummer et al., "Intraoperative detection of malignant gliomas by 5-aminolevulinic acid-induced porphyrin fluorescence," *Neurosurgery* **42**(3), 518–526 (1998).

16. C. G. Hadjipanayis, G. Widhalm, and W. Stummer, "What is the surgical benefit of utilizing 5-aminolevulinic acid for fluorescence-guided surgery of malignant gliomas?" *Neurosurgery* **77**(5), 663–673 (2015).

17. W. Stummer et al., "Fluorescence-guided surgery with 5-aminolevulinic acid for resection of malignant glioma: a randomised controlled multicentre phase III trial," *Lancet Oncol.* **7**(5), 392–401 (2006).

18. P. A. Valdes et al., "5-Aminolevulinic acid-induced protoporphyrin IX fluorescence in meningioma: qualitative and quantitative measurements in vivo," *Neurosurgery* **10**(Suppl. 1), 74–82 (2014).

19. M. Jaber et al., "The value of 5-aminolevulinic acid in low-grade gliomas and high-grade gliomas lacking glioblastoma imaging features: an analysis based on fluorescence, magnetic resonance imaging, 18F-fluoroethyl tyrosine positron emission tomography, and tumor molecular factors," *Neurosurgery* **78**(3), 401–411 (2016).

20. R. Diez Valle et al., "Surgery guided by 5-aminolevulinic fluorescence in glioblastoma: volumetric analysis of extent of resection in single-center experience," *J. Neurooncol.* **102**(1), 105–113 (2011).

21. G. Aldave et al., "Prognostic value of residual fluorescent tissue in glioblastoma patients after gross total resection in 5-aminolevulinic acid-guided surgery," *Neurosurgery* **72**(6), 915–921 (2013).

22. A. Nabavi et al., "Five-aminolevulinic acid for fluorescence-guided resection of recurrent malignant gliomas: a phase II study," *Neurosurgery* **65**(6), 1070–1077 (2009).

23. D. W. Roberts et al., "Glioblastoma multiforme treatment with clinical trials for surgical resection (aminolevulinic acid)," *Neurosurg. Clin. North Am.* **23**(3), 371–377 (2012).

24. G. Widhalm et al., "5-Aminolevulinic acid induced fluorescence is a powerful intraoperative marker for precise histopathological grading of gliomas with non-significant contrast-enhancement," *PLoS One* **8**(10), e76988 (2013).

25. M. Olivo and B. C. Wilson, "Mapping ALA-induced PPIX fluorescence in normal brain and brain tumour using confocal fluorescence microscopy," *Int. J. Oncol.* **25**(1), 37–45 (2004).

26. P. A. Valdes et al., "Quantitative fluorescence using 5-aminolevulinic acid-induced protoporphyrin IX biomarker as a surgical adjunct in low-grade glioma surgery," *J. Neurosurg.* **123**(3), 771–780 (2015).

27. S. Kaneko and S. Kaneko, "Fluorescence-guided resection of malignant glioma with 5-ALA," *Int. J. Biomed. Imaging* **2016**, 6135293 (2016).

28. Q. Peng et al., "5-Aminolevulinic acid-based photodynamic therapy: principles and experimental research," *Photochem. Photobiol.* **65**(2), 235–251 (1997).

29. R. M. Valentine et al., "Modelling fluorescence in clinical photodynamic therapy," *Photochem. Photobiol. Sci.* **12**(1), 203–213 (2013).

30. M. Marois et al., "Characterization and standardization of tissue-simulating protoporphyrin IX optical phantoms," *J. Biomed. Opt.* **21**(3), 035003 (2016).

31. J. T. Liu, D. Meza, and N. Sanai, "Trends in fluorescence image-guided surgery for gliomas," *Neurosurgery* **75**(1), 61–71 (2014).

32. S. L. Gibbs et al., "Protoporphyrin IX level correlates with number of mitochondria, but increase in production correlates with tumor cell size," *Photochem. Photobiol.* **82**(5), 1334–1341 (2006).

33. P. A. Valdes et al., "δ-aminolevulinic acid-induced protoporphyrin IX concentration correlates with histopathologic markers of malignancy in human gliomas: the need for quantitative fluorescence-guided resection to identify regions of increasing malignancy," *Neuro-Oncol.* **13**(8), 846–856 (2011).

34. R. Ishihara et al., "Quantitative spectroscopic analysis of 5-aminolevulinic acid-induced protoporphyrin IX fluorescence intensity in diffusely infiltrating astrocytomas," *Neurol. Med.–Chir.* **47**(2), 53–57 (2007).

35. J. T. Liu et al., "Dual-axes confocal reflectance microscope for distinguishing colonic neoplasia," *J. Biomed. Opt.* **11**(5), 054019 (2006).

36. J. T. Liu et al., "Efficient rejection of scattered light enables deep optical sectioning in turbid media with low-numerical-aperture optics in a dual-axis confocal architecture," *J. Biomed. Opt.* **13**(3), 034020 (2008).

37. L. K. Wong et al., "Improved rejection of multiply scattered photons in confocal microscopy using dual-axes architecture," *Opt. Lett.* **32**(12), 1674–1676 (2007).

38. B. Larson, S. Abeytunge, and M. Rajadhyaksha, "Performance of full-pupil line-scanning reflectance confocal microscopy in human skin and oral mucosa in vivo," *Biomed. Opt. Express* **2**(7), 2055–2067 (2011).

39. P. J. Dwyer, C. A. DiMarzio, and M. Rajadhyaksha, "Confocal theta line-scanning microscope for imaging human tissues," *Appl. Opt.* **46**(10), 1843–1851 (2007).

40. Y. Chen, D. Wang, and J. T. Liu, "Assessing the tissue-imaging performance of confocal microscope architectures via Monte Carlo simulations," *Opt. Lett.* **37**(21), 4495–4497 (2012).

41. D. Wang, Y. Chen, and J. T. Liu, "A liquid optical phantom with tissue-like heterogeneities for confocal microscopy," *Biomed. Opt. Express* **3**(12), 3153–3160 (2012).

42. J. T. Liu et al., "Micromirror-scanned dual-axis confocal microscope utilizing a gradient-index relay lens for image guidance during brain surgery," *J. Biomed. Opt.* **15**(2), 026029 (2010).

43. D. Meza et al., "Comparing high-resolution microscopy techniques for potential intraoperative use in guiding low-grade glioma resections," *Lasers Surg. Med.* **47**(4), 289–295 (2015).

44. Y. Chen et al., "Video-rate in vivo fluorescence imaging with a line-scanned dual-axis confocal microscope," *J. Biomed. Opt.* **20**(10), 106011 (2015).

45. C. Yin et al., "Miniature in vivo MEMS-based line-scanned dual-axis confocal microscope for point-of-care pathology," *Biomed. Opt. Express* **7**(2), 251–263 (2016).

46. D. Wang et al., "Comparison of line-scanned and point-scanned dual-axis confocal microscope performance," *Opt. Lett.* **38**(24), 5280–5283 (2013).

47. K. C. Maitland et al., "In vivo imaging of oral neoplasia using a miniaturized fiber optic confocal reflectance microscope," *Oral Oncol.* **44**(11), 1059–1066 (2008).

48. A. A. Tanbakuchi et al., "Clinical confocal microlaparoscope for real-time in vivo optical biopsies," *J. Biomed. Opt.* **14**(4), 044030 (2009).

49. A. A. Tanbakuchi et al., "In vivo imaging of ovarian tissue using a novel confocal microlaparoscope," *Am. J. Obstet. Gynecol.* **202**(1), 90.e1–90. e9 (2010).

50. B. F. Grewe et al., "High-speed in vivo calcium imaging reveals neuronal network activity with near-millisecond precision," *Nat. Methods* **7**(5), 399–405 (2010).

51. N. Bozinovic et al., "Fluorescence endomicroscopy with structured illumination," *Opt. Express* **16**(11), 8016–8025 (2008).

52. M. Kyrish et al., "Needle-based fluorescence endomicroscopy via structured illumination with a plastic, achromatic objective," *J. Biomed. Opt.* **18**(9), 096003 (2013).

53. F. Duffner et al., "Specific intensity imaging for glioblastoma and neural cell cultures with 5-aminolevulinic acid-derived protoporphyrin IX," *J. Neurooncol.* **71**(2), 107–111 (2005).

54. L. D. Stefano and A. Bulgarelli, "A simple and efficient connected components labeling algorithm," in *Proc. Int. Conf. on Image Analysis and Processing*, pp. 322–327 (1999).

Biographies for the authors are not available.